MIT Open Access Articles

Surface Plasmon#Enhanced Short#Wave Infrared Fluorescence for Detecting Sub#Millimeter#Sized Tumors

Surface Plasmon Enhanced Short-Wave Infrared Fluorescence for Detecting Submillimeter-Sized Tumors

Shengnan Huang, Ching-Wei Lin, Jifa Qi, Archana Mahadevan Iyer, Yanpu He, Yingzhong Li, Neelkanth M. Bardhan, Darrell J. Irvine, Paula T. Hammond, Angela M. Belcher*

S. Huang, Prof. D.J. Irvine, Prof. A.M. Belcher

Department of Materials Science and Engineering, Massachusetts Institute of Technology, Cambridge, MA, 02139, USA

E-mail: belcher@mit.edu

S. Huang, Dr. C-W Lin, [+] Dr. J. Qi, A.M. Iyer, Y. He, Dr. Y. Li, Dr. N.M. Bardhan, Prof. D.J. Irvine, Prof. P.T. Hammond, Prof. A.M. Belcher

The David H. Koch Institute for Integrative Cancer Research, Massachusetts Institute of Technology, Cambridge, MA, 02142, USA

Dr. J. Qi, Dr. N.M. Bardhan, Prof. D.J. Irvine, Prof. A.M. Belcher

Department of Biological Engineering, Massachusetts Institute of Technology, Cambridge, MA, 02139, USA

Y. He, Prof. P.T. Hammond

Department of Chemical Engineering, Massachusetts Institute of Technology, Cambridge, MA, 02139, USA

[+] Present address: Institute of Atomic and Molecular Sciences, Academia Sinica, Taipei, 10617, Taiwan

Keywords: surface plasmon, fluorescence enhancement, short-wave infrared, *in vivo* imaging

Short-wave infrared (SWIR, 900-1700nm) enables *in vivo* imaging with high spatiotemporal resolution and penetration depth due to the reduced tissue autofluorescence and decreased photon scattering at long wavelengths. Although small organic SWIR dye molecules have excellent biocompatibility, they have been rarely exploited as compared to their inorganic counterparts, mainly due to their low quantum yield. To increase their brightness, in this work the SWIR dye molecules are placed in close proximity to gold nanorods (AuNRs) for surface plasmon enhanced emission. The fluorescence enhancement is optimized by controlling the dye-to-AuNR number ratio and up to ~ 45-fold enhancement factor is achieved. In addition, the results indicate that the highest dye-to-AuNR number ratio gives the highest emission intensity per weight and this is used for synthesizing the SWIR imaging probes using layer-by-layer (LbL) technique with polymer coating protection. Then the SWIR imaging probes are applied for *in vivo* imaging of ovarian cancer and the surface coating effect on intratumor distribution of the imaging probes is investigated in two orthotopic ovarian cancer models. Lastly, it is demonstrated that the plasmon enhanced SWIR imaging probe has great potential for fluorescence imaging-guided surgery by showing its capability to detect submillimeter-sized tumors.

Fluorescence imaging has exceptional advantages over other imaging modalities, including low ionization dosage exposure, relatively low cost, real-time feedback, and high spatial and temporal resolution.[1–3] However, indocyanine green (ICG, emission ~ 800 nm) and methylene blue (MB, emission ~ 700 nm) are the only two clinically approved near-infrared (NIR) fluorophores. Although

their fluorescence peaks lie in the first near-infrared (NIR-I, 700-900 nm) window, which is far superior compared to visible wavelengths in terms of bioimaging, intensive efforts have recently been focused on imaging in the short-wave infrared (SWIR, 900-1700 nm) window due to the reduced tissue autofluorescence and decreased photon scattering at progressively longer wavelengths.[2,4–10] Hence, SWIR imaging has enabled imaging at centimeters depths.[4,6,11–13]

Current SWIR imaging moieties consist of mainly inorganic nanomaterials, including single-walled carbon nanotube (SWCNT), rare-earth doped down-conversion nanoparticle (DCNP), and quantum dot (QD), as their highly tunable electronic structures enable the synthesis of low-band gap semiconductors that emit SWIR photons.[14–18] However, those inorganic SWIR imaging moieties show disadvantages of low biocompatibility.[19,20] Recently, the development of small organic SWIR dye molecules has drawn great interest, because as compared to their inorganic counterparts, small organic dye molecules have salient advantages of outstanding biocompatibility and easy processability.[21,22] However, these small organic dyes suffer from low quantum yields and low photostability partly due to contact with surrounding quenching agents such as water molecules.[21] To address these issues, in this work gold nanorods (AuNRs) are used to enhance the emission of SWIR dye and the AuNR-dye nanocomposites are coated with polyelectrolytes (PEs) to protect them from the environment. AuNRs with appropriate aspect ratios provide strong local plasmon fields at wavelengths ranging from 800 to 1100 nm, matching either the excitation or emission wavelengths of our selected SWIR dye. In addition to enhancing the emission of the SWIR dye, the nano-size of the AuNR-dye nanocomposite may also facilitate the accumulation the SWIR dye in the targeted tissue.[23] Moreover, AuNRs have superior biocompatibility, are easy to synthesize, and have facile surface modifications, which all enable potential clinical diagnosis and treatments such as tumor

photothermal therapy and drug and gene delivery.[24–28] Although, detailed works have demonstrated using AuNRs for enhancing fluorescence in the visible and NIR-I region,[29–35] there are no reports on using AuNRs to enhance the fluorescence in the SWIR region. Hence, we demonstrate for the first time the use of AuNRs to enhance fluorescence in SWIR.

In order to optimize the plasmon enhancement, the effect of dye density on AuNR surface is studied. With the optimum dye surface density, layer-by-layer (LbL) technique is used to protect the AuNR-dye nanocomposite, forming a highly fluorescent SWIR imaging probe. LbL assembly of PE layers on a charged surface is a well-established technique for construction of functional thin films for applications of drug and gene delivery, and biosensing.[36–38] Then two murine models of disseminated ovarian cancer are established in athymic nu/nu female mouse and the plasmon enhanced SWIR imaging probes are administered for *in vivo* imaging of ovarian cancer via intraperitoneal (i.p.) injection. i.p. administration is chosen as it shows higher efficacy of delivering nanoparticles and chemotherapeutic drugs to ovarian cancer nodules than intravenous (i.v.) administration, possibly due to the proximity effect and avascular nature of small ovarian cancer metastases.[39–41] Next, how the surface coating of the imaging probes changes their intratumor distributions is investigated in the two orthotopic ovarian cancer models, namely SKOV-3 and OVCAR-8. Finally, it is demonstrated that the plasmon enhanced SWIR imaging probe is able to locate submillimeter-sized tumors, making it a good candidate for fluorescence imaging-guided surgery. Prior work has demonstrated the effectiveness of surface plasmon enhanced NIR-I fluorescence for *in vivo* imaging,[42,43] however, this study is the first report of using plasmon enhanced SWIR fluorescence for *in vivo* imaging, to the best of our knowledge.

A commercially available small organic SWIR dye, IR-E1050, which has an absorption peak at ~ 770 nm and an emission peak at ~ 1000 nm as shown in **Figure 1**a, is selected for this study. The emission of the small SWIR dye can be enhanced by excitation rate enhancement or radiative decay rate enhancement, depending on whether the extinction spectrum of the AuNRs overlaps with the absorption spectrum or the emission spectrum of the SWIR dye, respectively.

Based on the absorption spectrum of the SWIR dye, laser with wavelength of 808 nm was used as the excitation source. As photothermal ablation of tissue is reported when exciting the AuNRs at their localized surface plasmon resonance (LSPR) wavelength, possible tissue damage can happen if we use AuNR808 with LSPR peak matching the excitation wavelength to enhance the emission.[44] Therefore, in this study, gold nanorod 980 (AuNR980) with extinction spectrum overlapping mostly with the emission spectrum of the SWIR dye (Figure 1a, red solid line) is selected for fluorescence enhancement of the SWIR dye via mainly radiative decay rate enhancement.[45] The AuNR980 was initially coated with citrate molecules. The dye molecules were assembled on the AuNR980 surface along with another wrapping layer of sodium polystyrene sulfonate (PSS), forming a SWIR fluorescent AuNR980-dye nanocomposite as shown in the scheme in Figure 1b. The SWIR dye emission center may be separated from the AuNR980 surface by the spacer units in the molecular structure.[22] PSS is used because it can preferentially interact with the SWIR dye possibly via hydrophobic interactions,[46] and it offers the colloidal stability of the AuNR980-dye nanocomposite (see Figure S1 for more details). The dye/PSS layer is around 2-3 nm as shown in the transmission electron microscope (TEM) image in Figure 1b. Our previous study has demonstrated that the intensity of plasmon enhanced fluorescence changes with dye surface density on the plasmonic nanostrucures.[47] Therefore, in this study, the AuNR-dye emission is optimized by tuning the dye-to-

AuNR stoichiometric ratio. The dye density on the AuNR surface was varied by changing the amount of total dye molecules in the reaction solution while keeping the amount of AuNRs constant. By using the fluorescence method, the number of dye molecules adsorbed on the AuNR980 surface was calculated after subtracting the unbound dye molecules from the total dye molecules (see Figure S2). As the LSPR wavelength of AuNR is very sensitive to the refractive index changes of its surface coating, the change of the dye density on the AuNR980 surface can be well monitored by measuring the shifts of the LSPR wavelength.[48] As shown in Figure 1c (red empty square, see detailed absorption spectrum in Figure S3a), the results indicate that the LSPR wavelength or the absorption peak of the AuNR980-dye nanocomposites redshifts with increasing dye density on AuNR980 surface and reaches plateau at ~ 5000 copies of dye molecules per AuNR980. The redshift of the LSPR wavelength indicates increased refractive index at higher dye surface density and the plateau indicates the saturation of the dye adsorption on the AuNR980 surface. In addition, there is little LSPR peak damping with increasing dye density as shown in Figure S3c. A similar trend is also observed for the emission peak of the AuNR980-dye nanocomposite (Figure 1c, blue empty sphere, see detailed emission spectrum in Figure S3d), which may originate from the increased nonradiative energy transfer among adjacent dye molecules as a result of the decreased inter-dye distance.[49] Moreover, the emission peak of the AuNR980-dye nanocomposites blueshifts as compared to free dye (inset in Figure S3d), which could be ascribed to the selective plasmon-dye coupling that modifies the emission spectrum.[50] Next, the emission intensity and the enhancement factor of the AuNR980-dye nanocomposite were studied as a function of dye density on AuNR980 surface. The detailed enhancement factor calculation can be found in Supporting Information section S4. As shown in Figure 1d, the emission photon rate (number of photons emitted per second, blue empty

6

square, excitation: 808 nm, emission: 1000 nm with 50 nm bandwidth) increases with the dye surface density and then flattens out due to the saturated dye adsorption. Moreover, the enhancement factor (red empty circle) increases and then decreases as the dye density increases, with a peak enhancement factor of ~ 45-fold. In our previous study, it was reported that the enhancement factor increases monotonically with increasing dye surface density and this is attributed to the decreased dye quantum yield at increased surface density.[47] Although it may appear inconsistent with the previous report, in the present study it is hypothesized that the quantum yield of the SWIR dye decreases with increasing density on the AuNR980 surface for the same reason as discussed in Figure 1d. In current study, the dye-to-AuNR distance may depend on the dye surface density, whereas it was kept constant in the previous study. The dye-to-AuNR distance may increase with increasing dye surface density in current work. It has been shown that the enhancement factor increases and then decreases with increasing dye-to-metal nanoparticle distance,[51] similar to the dependence of enhancement factor on the dye surface density observed in this work. Hence, the dependence of the enhancement factor on the SWIR dye surface density in this work may be explained by the dominant effect of the increased dye-to-AuNR distance on the enhancement factor over that of the lowered quantum yield (see Figure S5 for the detailed explanation). However, this needs further study. As low dosage of nanomaterial imaging probes is preferred for *in vivo* administration, it is essential to find the optimal dye density that gives the highest emission intensity on the weight basis. As shown in Figure 1e, the highest intensity per weight (combined weight of the dye and the AuNR) is achieved when the dye adsorption saturates (~ 5000 copies) on the AuNR surface. Hence, this dye-to-AuNR ratio is chosen for all further work, for synthesizing plasmon enhanced SWIR imaging probes.

With the optimal dye-to-AuNR ratio as determined above, the coatings of the AuNR-dye nanocomposite are then engineered to allow for *in vivo* imaging of ovarian cancer. LbL method was adopted to assemble the imaging probes using PSS and polyethyleneimine (PEI) as the negatively and positively charged poly electrolyte (PE) layers, respectively. PEI is chosen due to its high positive charge density, but meanwhile this raises the concern of its toxicity. Hence, *in vitro* cell toxicity of the AuNR-dye nanocomposites with the PEI coating was first evaluated, and minimal toxicity effects were detected (see Figure S6), thereby negating the toxicity concern of PEI. Three types of plasmon enhanced SWIR imaging probes, namely, PSS-terminated, mPEG-terminated, and FA-terminated, based on their outmost coatings as shown in Figure 1f, were then synthesized and compared. Using the PSS-terminated probes as reference, the mPEG-terminated probes are coated with polyethylene glycol (mPEG, molecular weight 5000g/mol) on top of the PSS-terminated probes because mPEG is widely exploited to decrease the nonspecific interactions between nanoparticles and biological environment.[52] For FA-terminated imaging probes, PEG-folic acid (PEG-FA, molecular weight 5000g/mol) is coated instead of mPEG in order to actively target the ovarian cancers that overexpress folate receptor (FR), for example, SKOV-3 cell line in this study.[53] Figure 1g shows that the LSPR wavelength of AuNR980 redshifts upon addition of either the successive PE layer or the PEG layer. In addition, zeta potential reveals the inversion of charge polarity upon successive coating of the PE layer (Figure 1h). The PSS-terminated imaging probes have a zeta-potential of ~ −30 mV. Upon further modification with mPEG (mPEG-terminated), the zeta potential drops to around ~ −13 mV due to the charge shielding effect of mPEG. As folic acid has negative charge, the zeta potential of the FA-terminated imaging probe is ~ −18 mV, which is slightly more negative than that of the mPEG-terminated imaging probes. The results in Figure 1g and 1h indicate that the desired materials

8

are successfully coated onto the reference imaging probes. Then the emission intensity of the imaging probes was evaluated, showing no degradation in fluorescence upon exposure to biological environment (see Figure S7 for details). Apart from the enhanced emission, another advantage of plasmon enhanced fluorescence is the increased photostability of the fluorophores due to the shortened lifetime,[34,54] which reduces the time for the excited-state photodestruction to occur.[55] This is demonstrated by comparing the photobleaching of free dye and AuNR-dye nanocomposites with 1 layer, 3 layers and 5 layers of PE coatings. As shown in Figure 1i, after 4 hours of continuous laser excitation (808 nm), the emission intensity of free dye drops to half of its initial value, whereas that of the AuNR-dye nanocomposites remains close to 80%. In addition, the photostability of the AuNR-dye nanocomposite increases slightly with the number of PE layers, which could be ascribed to the decreased dye-water interactions.

Next, the cancer targeting capability of the three types of imaging probes is compared in an orthotopic ovarian cancer model established with human ovarian cancer cell line of SKOV-3. SKOV-3 is chosen because it is genetically similar to high grade serious ovarian cancer (HGSOC). Orthotopic ovarian cancer was established in immunocompromised female nu/nu mice normally two weeks after i.p. injection of cancer cells. Imaging probes with three different surface coatings as in Figure 1f were i.p. injected at a single dosage of ~ 15 μg per mouse (~ 0.6 mg kg^{-1}), which is tens to hundreds times lower than previously reported for *in vivo* imaging of ovarian cancer with hard-core nanoparticles via either i.p. or i.v. injection.[15,39,56] SWIR fluorescence images of the whole body, the excised organs, and tumor nodules were captured 24 hours post injection of the imaging probes as in **Figure 2**a-c. As the used SKOV-3 cell line has been engineered to express reporters of luciferase, it is possible to colocalize the imaging probes with the ovarian cancer by comparing the SWIR

fluorescence signal from the imaging probes and the bioluminescence signal from the cancer cells. The bioluminescence and the SWIR fluorescence signals from *in vivo* whole animal, *in vivo* exposed abdomen, *ex vivo* excised organs and *ex vivo* excised tumors show that both the passive targeted (PSS-termianted and mPEG-terminated) and the active targeted (FA-terminated) imaging probes are able to detect individual disseminated tumor nodules and tumor nodules on peritoneal organs with minor accumulation in normal tissue (see also Figure S8). This is consistent with the previous findings that nanoparticles accumulate in ovarian cancer nodules even without targeting ligands.[39,57] It is also worth noting here that the dosage of the current imaging probes did not cause any detectable toxicity during the imaging period, as shown by histology images of the major organs in Figure S9. This finding further eases the toxicity concern of PEI used in our imaging probes for this study.

Even though all the three types of imaging probes offer promising ovarian cancer imaging capabilities, it is important to investigate whether they have different intratumor distributions in the SKOV-3 ovarian cancer model. The tumor nodules of interest were fixed and then stained with hematoxylin and eosin (H&E) and were examined under our home-built SWIR fluorescence microscope (excitation: 850 nm, emission: 1000 nm with 50 nm bandwidth). As shown in the first column of Figure 2d-f, the formation of orthotopic ovarian tumors is characterized by the large nuclear-to-cytoplasmic ratio, irregular cell shape, crowded cell packing and necrotic core (labelled as T). In addition, the SWIR fluorescence of the imaging probes allows for colocalization of the imaging probes with tumor tissue at the cellular level. The results show that all the three types of imaging probes are primarily located at the tumor periphery with limited tumor tissue penetration as shown in the third column of Figure 2d-f (green color). Furthermore, based on the histological features of the cells that colocalize with the imaging probes, it is postulated that the imaging probes are

predominantly phagocytosed by tumor associated macrophages (labelled as M). This is further confirmed by immunohistochemistry (IHC) staining of the tumor nodules with murine pan-macrophage marker F4/80 as shown in Figure 2g-i (see individual channel images in Figure S10). As gold nanoparticles have large absorption cross-section and their refractive index is different from the surrounding biological tissue,[58] optical imaging has been used to study the distribution of gold nanoparticles in biological samples. Hence, the imaging probe clusters are visualized as dark spots under the bright field of the optical microscope and they are false colored in green in Figure 2g-i.[57,59] This is also confirmed by the colocalization of the SWIR signal from the imaging probes with their bright field image as in Figure S11. Overlap of the imaging probes (green color) and the anti-mouse F4/80 antibody (red color) provides additional evidence that the three types of imaging probes are primarily phagocytosed by macrophages that reside at the edge of the tumor nodules. A similar nanoparticle intratumor distribution is also observed by Korangath *et al.*, where they find nanoparticles are primarily taken up by tumor associated immune cells residing in tumor periphery.[60] In addition, the insignificant difference in the intratumor distribution of the three types of imaging probes also suggests that some of the interactions between the SKOV-3 cancer cells and the imaging probes may be nonspecific.[57] Moreover, the finding that the SWIR imaging probes are phagocytosed by tumor associated macrophages may explain the previous observations that nanoparticles preferentially accumulate in tumor tissue even without active targeting; irrespective of the surface coating used.

To further study the tumor targeting pathways of the plasmon enhanced SWIR imaging probes, the imaging probes were tested in a second orthotopic ovarian cancer model established with OVCAR-8 human ovarian cancer cell line. The objective is to compare the response of different tumor models

to the same imaging moiety. Passive targeted (PSS-terminated) imaging probes were used for this experiment. Bioluminescence and SWIR fluorescence images of *in vivo* whole animal, *in vivo* exposed abdomen and *ex vivo* tumor nodules and peritoneal organs are summarized in **Figure 3**a. Matched patterns between the bioluminescence and the SWIR fluorescence images suggest that the imaging probes can detect individual disseminated tumor nodules and tumor nodules on the peritoneal organs, similar to the SKOV-3 ovarian cancer model. However, the intratumor distribution of the imaging probes in OVCAR-8 ovarian cancer differs from that in SKOV-3 ovarian cancer in two aspects. First, the imaging probes are able to penetrate ~ 100-200 µm deeper into the OVCAR-8 ovarian cancer as compared to SKOV-3 ovarian cancer as shown in the H&E stained histology slides (Figure 3b vs. Figure 2d). Second, the cellular level distribution of imaging probes in the two ovarian cancer models are different. In the SKOV-3 ovarian cancer, the imaging probes are primarily phagocytosed by macrophages in tumor periphery. In contrast, in the OVCAR-8 ovarian cancer, it is observed that the imaging probes infiltrate into the tumor mass and enter OVCAR-8 cancer cells based on the morphology of the cancer cells. Since macrophages are competing with cancer cells in nanoparticle uptake,[57] the difference in intratumor distribution indicates that OVCAR-8 cancer cells may take up the imaging probes more rapidly than macrophages or less percentage of macrophage populations exists in OVCAR-8 tumor microenvironment than in SKOV-3. Further study needs to be done to find out the possible reasons.

The plasmon enhanced SWIR fluorescence imaging probes are good candidates for fluorescence imaging-guide surgery for the following two reasons. First, they are able to help remove smaller tumors that surgeons cannot locate by eyes, because their SWIR emission has deeper tissue penetration, low tissue scattering and low tissue autofluorescence. This is an attractive feature for

ovarian cancer since thorough tumor debulking could greatly increase patients' survival rate.[41] Second, the imaging probes have high photostability as discussed in Figure 1i, so they are able to last through the period of tumor resection and margin assessment. In the peritoneal cavity, the primary metastatic sites for ovarian cancers are the surface of peritoneal organs,[61] hence, intestine along with the connecting mesentery is the preferential site for ovarian cancer metastases. **Figure 4**a shows the bioluminescence and the SWIR images of the intestine in the region of interests (full view in Figure S12). This study was performed using PSS-terminated imaging probes with SKOV-3 ovarian cancer model. The bioluminescence image shows tiny ovarian cancer metastases at the intestine or mesentery surfaces labeled as 1-8. These tiny metastases were located in the SWIR images accordingly. The observed lower signal-to-background ratio (SBR) of metastases labelled 5-8 as compared to that of 1-4 may originate from the inhomogeneous excitation power density; the excitation power is higher in the center (metastases 1-4) than at the edge (5-8). With *in situ* florescence imaging-guided resection, it was possible to locate the area of interest indicated by the yellow dashed rectangle in the SWIR image (Figure 4a). Post euthanasia and resection, this tissue was fixed and then stained with H&E for tumor size analysis as shown in Figure 4b. The metastases in Figure 4a are labelled accordingly in Figure 4b. From the H&E image, metastasis 1 is measured to be ~ 550 μm and metastasis 2 is measured to be ~ 900 μm in diameter. In addition, the imaging probes are also able to detect submillimeter-sized metastases in the OVCAR-8 ovarian cancer model as shown in Figure S13. Taking these results into consideration, the plasmon enhanced SWIR imaging probe enables the detection of submillimeter-sized ovarian cancer metastases, which makes it an excellent candidate for real-time fluorescence imaging-guided surgery.

In conclusion, plasmon enhanced SWIR fluorescence imaging probes with high brightness have been developed, allowing for *in vivo* imaging of ovarian cancer down to submillimeter in size. To the best of our knowledge, this is the first report on plasmon enhanced SWIR fluorescence for *in vivo* imaging applications. AuNR980 was used to enhance the fluorescence of a SWIR dye via mainly radiative decay rate enhancement. The effect of dye-to-AuNR ratios on the absorption peak, emission peak and emission brightness for the AuNR980-dye nanocomposite was studied. The results show that the highest emission intensity per weight occurs when the dye density on the AuNR980 surface saturates. With LbL coatings, the plasmon enhanced SWIR imaging probes were synthesized and were applied for *in vivo* imaging of ovarian cancers. The surface coating effect of imaging probes (PSS-terminated, mPEG-terminated and FA-terminated) on their intratumor distributions was investigated in two orthotopic ovarian cancer models: SKOV-3 and OVCAR-8. Both passive targeted (PSS-terminated, mPEG-terminated) and active targeted (FA-terminated) imaging probes are able to locate ovarian cancers and they have similar intratumor distributions in the SKOV-3 cancer model, namely, they colocalize with the macrophages at the periphery of the tumor tissue. However, for the case of OVCAR-8, the PSS-terminated imaging probes are able to penetrate into the tumor mass and enter the cancer cells. Lastly, the plasmon-enhanced imaging probes are shown to be excellent candidates for fluorescence imaging-guided surgery by demonstrating the ability to detect submillimeter-sized ovarian cancer nodules.

Experimental Section

Materials and Reagents. IR-E1050-COOH(NIRMIDAS Biotech, Palo Alto, CA, USA), Poly(styrene sulfonic acid) sodium salt(70kDa, Sigma Aldrich, St. Louis, MO, USA), branched polyethylenimine (70kDa, 30% w/v, Polysciences, Warrington, PA, USA), gold nanorod (Nanocomposix, San Diego, CA,

USA or Nanopartz, Loveland, CO, USA), Succinimidyl PEG5000-NHS (mPEG-NHS, Nanocs, New York, NY, USA), Folic Acid-PEG5000-NHS (FA-PEG-NHS, Biochempeg, Watertown, MA, USA), PE-antimouse F4/80 Antibody(Clone: BM8, Biolegend, San Diego, CA, USA,), OCT compound (Fisher Healthcare Tissue-Plus O.C.T. Compound, Fisher Scientific, Houston, TX, USA)

Synthesis of the Imaging Probes with LbL. The surface of the AuNR was initially coated with citrate molecules. The IR-E1050 dye (1mg/mL in PBS1×) was mixed with AuNR solution. Then the PSS solution (70kDa; 2mg/mL of 1 mM NaCl$_{(aq)}$) was added to the above AuNR-dye solution. After incubating at room temperature for 1 h, the solution was then centrifuged at 6 krpm for 30 min followed by removal of the supernatant.To calculate the amount of dye attached to the AuNRs, the top suspension of the AuNR-dye/PSS was centrifuged again at 14 krpm for 30 min and half of the top suspension was retrieved for later measurement of the dye quantity using fluorescence method.

The remaining product from above, AuNR-dye/PSS, were then redispersed in 1mM NaCl$_{(aq)}$. This AuNR-dye/PSS solution was added to a branched PEI solution (2mg/mL of 1mM NaCl$_{(aq)}$) and was reacted for 4 h at room temperature. The resulting AuNR-dye/PSS/PEI product was again centrifuged at 6 krpm and then was redispersed in 1mM NaCl$_{(aq)}$. The above step was repeated to coat the third layer with PSS, yielding the final product, AuNR-dye/PSS/PEI/PSS.

The mPEG/FA-terminated imaging probes were synthesized by reacting the AuNR-dye/PSS/PEI/PSS with mPEG-NHS/FA-PEG-NHS via EDC/NHS crosslinking reaction in 10mM HEPES solution overnight. The crosslinking reaction occurs between the free amines in the PEI and the NHS ester groups in the mPEG-NHS/FA-PEG-NHS molecules. Although the outer PSS layer may limit the availability of free amines for crosslinking reaction, it is highly likely that there are still some free amines available for

the crosslinking reaction considering that branched PEI has high amine density. The number ratio between the PEG molecules and the AuNRs is $10^4 : 1$, namely, 10^4 PEG molecules per AuNRs. The large excess of PEG molecules ensures maximum PEG coating on the AuNR surface. After reaction, the excess PEG molecules are removed by centrifuge twice (6krpm, 30min).

Optical Characterization. The absorption spectrum of the dye and the extinction spectrum of AuNRs were measured using a UV-vis spectrophotometer (DU800, Beckman-Coulter) with solution volume of 120 μL and cell path length of 10 mm. The fluorescence spectrum of the imaging probes was measured with a liquid nitrogen cooled single-element InGaAs detector on NanoLog spectrofluorometer (Horiba Jobin Yvon Inc.). The solution volume was 100 μL and cell path length was 10 mm. An 850 nm longpass filter (FELH850, Thorlabs) was installed in the emission path to eliminate the second order emissions from the excitation source. The excitation sources are either a continuous-wave 808 nm laser (CNI Laser) for emission spectrum measurements. or a wavelength-tunable femtosecond laser (690 nm – 1040 nm; MaiTai HP, Spectra Physics).

Photostability Study. For the photostability test, all of the AuNR980-dye samples (1,3, 5 layers of polyelectrolytes) had OD at LSPR wavelength of 0.1. The concentration of the free dye sample was 0.6 μM. They were under continuous illumination of 808 nm (continuous-wave 808 nm laser). The laser power was ~ 320 mW. The emission intensity at 970 nm was recorded every 1min for up to 4 hours.

TEM Characterization. The transmission electron microscope (TEM) images of the LbL-coated AuNRs were taken using a JEOL 2010 Advanced High Performance TEM.

Zeta Potential Measurement. Zeta potential of the nanoparticles are measured with the the Malvern ZS90. Nanoparticle solutions were diluted in 1mM NaCl(aq) solution in DTS1070 folded capillary cuvettes (Malvern) for zeta potential characterization

Mouse Handling and Imaging Probe Injection. All animal experiment procedures and protocols were pre-approved by the Division of Comparative Medicine (DCM) and the Committee on Animal Care (CAC) under the protocol #0219-004-22, Massachusetts Institute of Technology, and in compliance with the Principles of Laboratory Animal Care of the National Institutes of Health (NIH), United States of America.

Female athymic nu/nu mice (4-6 weeks old) were purchased from Charles River and AIN-76A purified diet was purchased from TestDiet. Mice were kept on AIN-76A diet for at least one week prior to *in vivo* imaging experiments to reduce food-related autofluorescence. Immediately before whole-body imaging, the mice received single dose of the imaging probes (~ 75 µg/mL, ~ 0.9 nM, 200µL, PBS1×) *via* intraperitoneal (i.p.) injection.

Cell Culture and Establishment of an Orthotopic Ovarian Cancer Model. SKOV-3 or OVCAR-8, was grown in RPMI 1640 medium supplemented with 10% FBS and 1% penicillin/streptomycin under 5% CO_2 at 37 °C. Both cell lines (provided by Paula Hammond's laboratory, Koch Institute, MIT) were transduced with luciferase. To establish an orthotopic ovarian tumor model, SKOV-3/OVCAR-8 cells (2×10^6 in 200 µL of PBS1×) were implanted into the peritoneal cavity of female athymic nu/nu mice. The tumor growth was monitored by imaging bioluminescence signals using the IVIS imaging instrument (PerkinElmer). For bioluminescence measurements, 200 µL of luciferin (PerkinElmer) solution in PBS 1× (15 mg/mL) were administered to each animal by IP injection. After 10 mins, the

mice were imaged for bioluminescence signal. The bioluminescence images were processed using the Living Imaging Software (PerkinElmer).

RAW 264.7 cell line is a gift from Prof. Jiahe Li (Northeastern University). RAW 264.7 cells were cultured in DMEM medium supplemented with 10% FBS and 1% penicillin/streptomycin under 5% CO_2 level at 37 °C

Detection of Orthotopic Ovarian Tumors. After ~ 14 days of IP implant of SKOV-3 cells, the ovarian cancers formed and disseminated in the peritoneal cavity and was confirmed by bioluminescence imaging. Then, the mice received a single dose of imaging probes (~ 75 µg/mL, 200 µL, PBS1×) intraperitoneally. Immediately following the IP injection, the whole-body fluorescence images were acquired when the mouse was under anesthesia. the whole-body bright field images and fluorescence images were collected at multiple time points from 5min to 96 h post injection. the mice were euthanized at 96 h post injection, and the tumor tissue was collected with facilitation of the SWIR fluorescence imaging and the bioluminescence imaging. The collected tumor tissues and organs were fixed with 10% formalin and sectioned for H&E staining and immunohistochemical staining. For the control experiments, healthy female nude mice received a single dose of imaging probes (~ 75 µg/mL, 200 µL, PBS1×) *via* IP injection. Then the same procedures were followed as described above.

Animal Imaging at SWIR. The *in vivo* and *ex vivo* images were collected using a home-built SWIR imager. The mouse was placed on the imaging platform and excited at 808 nm with a power density of ~ 100 mW/cm². The fluorescence signals were first transmitted through a filter set (FELH850, Thorlabs + #87-811, Edmund optics) for wavelength selection and then focused by a lens (SWIR-25,

Navitar) for image acquisition on the InGaAs camera. For bright field imaging, the specimen was illuminated with a Halogen lamp and the images were collected using the InGaAs camera with a 900 nm bandpass filter. The acquired images were postprocessed using a custom script written in MATLAB program. In brief, the recorded amplitudes were multiplied by the acquisition time to obtain real emission intensities. The intensities were multiplied to reach maximum contrast, with which were then tuned to the same level for intensity comparison among the images. The threshold was set to ten percentiles for overlaid images.

Tissue Slice Imaging. The SWIR fluorescence images of the histology slides were taken using a custom-built SWIR fluorescence microscope. The tissue of interest was fixed in 10% formalin solution overnight at 4 °C. The tissue were then sectioned at a thickness of 5 μm. The histology slides were H&E stained before imaging. We used a SWIR compatible objective (LD C-Apochromat 40x/1.1, Zeiss) to focus the excitation onto the region of interest and collect its emission. The laser beam at 850 nm (690 nm – 1040 nm; MaiTai HP, Spectra Physics) was expanded by a 5x beam expander (GBE05-B, Thorlabs) and then refocused into a high-power multimode optical fiber (MHP550L02, Thorlabs) using a reflective mirror (RC04SMA-P01, Thorlabs). The laser transmitted to the other end of the fiber was then refocused to form a semi-parallel beam using another reflective mirror (RC02SMA-P01, Thorlabs). A 950-nm filter cube (DMLP950R, FESH0950, and FELH0950 in DFM1, Thorlabs) then reflected the laser beam into the objective. The collected emission was transmitted through the same filter cube. After that, a scanning lens (TTL200-S8, Thorlabs) was used to refocus the emission beam, which was then directed to either the InGaAs camera for near infrared emission or a color camera (Q-color 3, Olympus) for imaging H&E stained tissue. An extra bandpass filter set was used to select the appropriate emission wavelengths for near infrared imaging. All H&E stained

19

slides were also scanned using a digital whole slide scanner (Aperio AT2, Leica Biosystems). The image processing including contrast tuning and image overlay was performed using a custom-built MATLAB program.

Immunohistochemical (IHC) Staining of Tissue Slices. The tissue of interest was snap frozen by embedding the tissue into the OCT compound in a cryomold (Tissue-Tek). The cryomold was then place onto an aluminum block which was almost completely immersed into liquid nitrogen (the surface of the aluminum block is free of liquid nitrogen) and waited for about 10 min. The cryomolds were maintained at -80 °C until they could be cryosectioned by the Koch Institute's histology core facility. The tissue slices (5 μm thickness) of interest were IHC stained with antimouse F4/80 antibody and DAPI. The IHC stained tissue slides were imaged with the Nikon A1R Ultra-Fast Spectral Scanning Confocal Microscope of the Koch Institute's microscope core facility using the PE, DAPI and bright field channels. The images of individule channels are processed using the ImageJ software.

Supporting Information

Supporting Information is available from the Wiley Online Library or from the author.
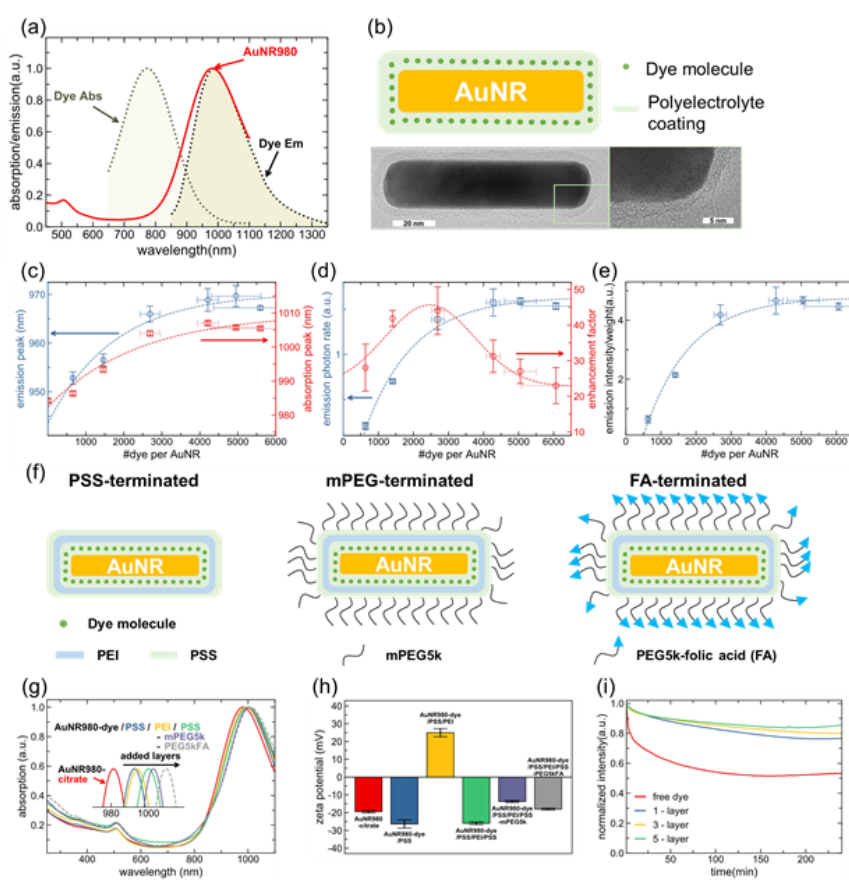
Acknowledgements

Figure 1. Optimization of the plamson enhancement and synthesis of the AuNR980-dye nanocomposite. (a). The relative position of the SWIR dye absorption (dotted grey line), emission (dotted black line), and AuNR980 (red line) extinction spectrum as normalized by the peak absorption or emission. (b). Scheme and TEM image of the AuNR980-dye nanocomposite. (c). Emission peak (blue empty sphere) and absorption peak (red empty square) of the AuNR980-dye nanocomposite. (d). Emission photon rate (blue empty square) and enhancement factor (red empty sphere) of the AuNR980-dye nanocomposite. (e). Emission intensity per weight of the AuNR980-dye nanocomposite. (f). Three designs of the imaging probes: PSS-terminated, mPEG-terminated and FA-terminated. (g). Normalized (by the maximum absorption) absorption and (h) zeta potential of the imaging probes with successive PE layer coating, mPEG and FA-PEG modification. (i). Photostability of free dye (red) and the imaging probe with 1(blue line) layer, 3 (orange line) and 5 (green line) PE layers. Error bar in (c-e) and (h) is the standard deviation. (d) and (e) are calculated at emission wavelengths centered at 1000 nm with 50 nm bandwidth. Dotted lines in (c-e) are for guidance only.
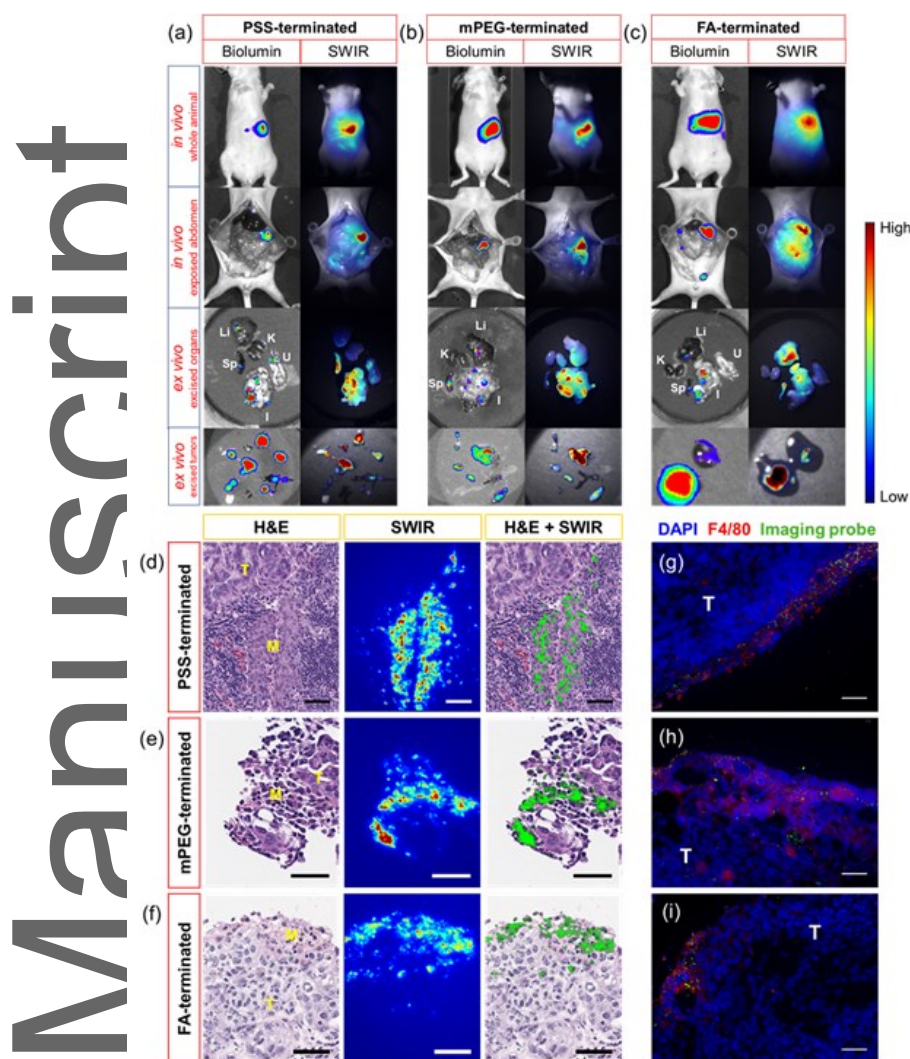
Figure 2. *In vivo* imaging of SKOV-3 ovarian cancer using three types of imaging probes. Bioluminescence (Biolumin) and SWIR fluorescence images (overlapped with bright field images) of *in vivo* whole animal, *in vivo* exposed abdomen, *ex vivo* excised organs and *ex vivo* excised tumors imaged by (a) PSS-, (b) mPEG- and (c) FA-terminated imaging probes. Histology slides of tumor nodules detected by (d) PSS-, (e) mPEG- and (f) FA-terminated imaging probes are examined under SWIR fluorescence microscope. IHC staining showing macrophage phagocytosis of the imaging probes in tumor nodules imaged by (g) PSS-, (h) mPEG- and (i) FA-terminated imaging probes. The slides are stained with DAPI (blue) and F4/80 (red). The bright field image of AuNRs are false colored as green color in (g-i). Li: liver, Sp: spleen, I: intestine, K: kidney, U: uterus, M: macrophage, T: cancer cells. Color bar of the SWIR fluorescence images in (a-f) and the bioluminescence images in (a-c) is shown in the right. Scale bar of (d-i) is 50 μm.
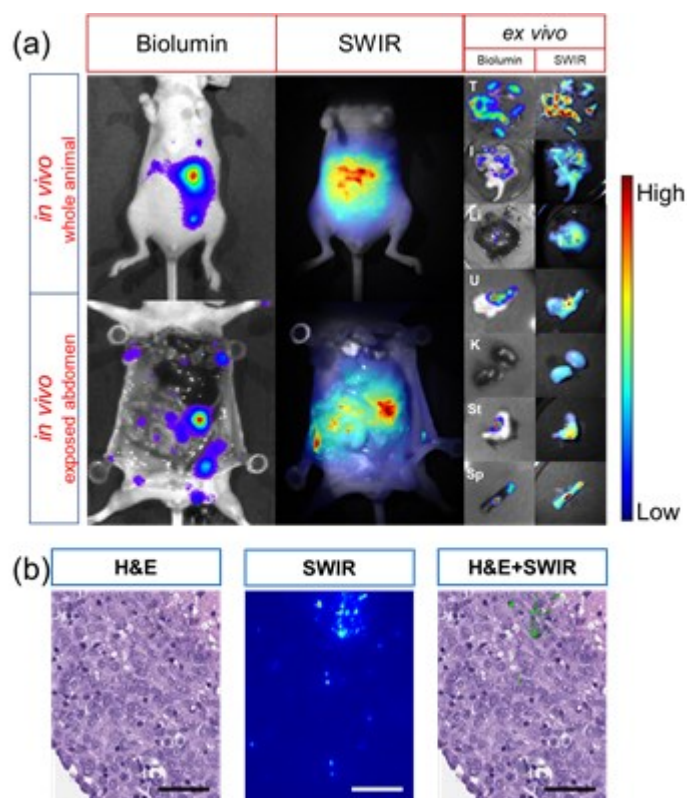
23

Figure 3. *In vivo* imaging of OVCAR-8 ovarian cancer with PSS-terminated imaging probes and intratumor distribution of the imaging probes. (a). Bioluminescence (Biolumin) and SWIR fluorescence images (overlapped with bright field images) of the *in vivo* whole animal, *in vivo* exposed abdomen and *ex vivo* excised tumor nodules and organs show good match. Color bar of the SWIR fluorescence image and the bioluminescence image is shown in the right. (b). Intratumor distribution of the imaging probes in the tumor tissue; first column shows the H&E stained bright field image, second column shows the SWIR fluorescence image of the imaging probes (color bar as in (a)), and third column shows the overlapped image of the bright field and fluorescence image (green color). Scale bar is 50 μm.
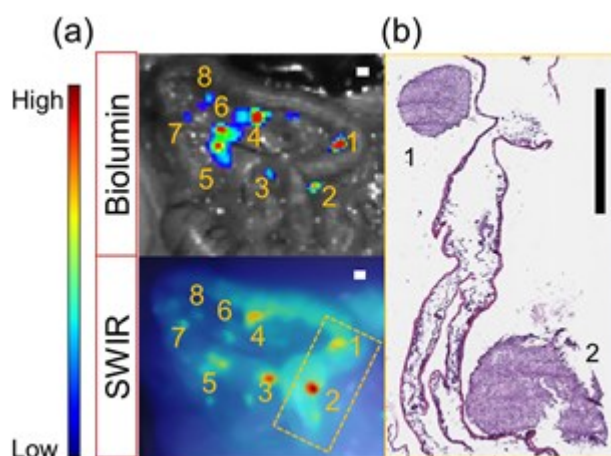
Figure 4. Detection of submillimeter-sized ovarian cancer metastases on intestine in SKOV-3 ovarian cancer model with PSS-terminated imaging probes. (a). Bioluminescence (Biolumin) and SWIR fluorescence image (overlapped with bright field images) of tumor nodules. Color bar of the SWIR fluorescence image and the bioluminescence image is shown in the left. (b). H&E stained bright field image shows the enlarged view of the yellow dashed line region in (a). Scale bar is 1mm.

A surface plasmon enhanced short-wave infrared (SWIR) fluorescent probe with high brightness is developed. Both the actively targeted and passively targeted imaging probes can locate tumors *in vivo* with similar intratumor distributions in the SKOV-3 ovarian cancer model. In addition, the plasmon enhanced SWIR imaging probes are able to detect submillimeter-sized tumor nodules, making them excellent candidates for fluorescence imaging-guided surgery.

Short-wave infrared fluorescence enhancement

S. Huang, C-W Lin, J. Qi, A. M. Iyer, Y. He, Y. Li, N. M. Bardhan, D. J. Irvine, P. T. Hammond, A. M. Belcher*

Surface Plasmon Enhanced Short-Wave Infrared Fluorescence for Detecting Submillimeter-Sized Tumors
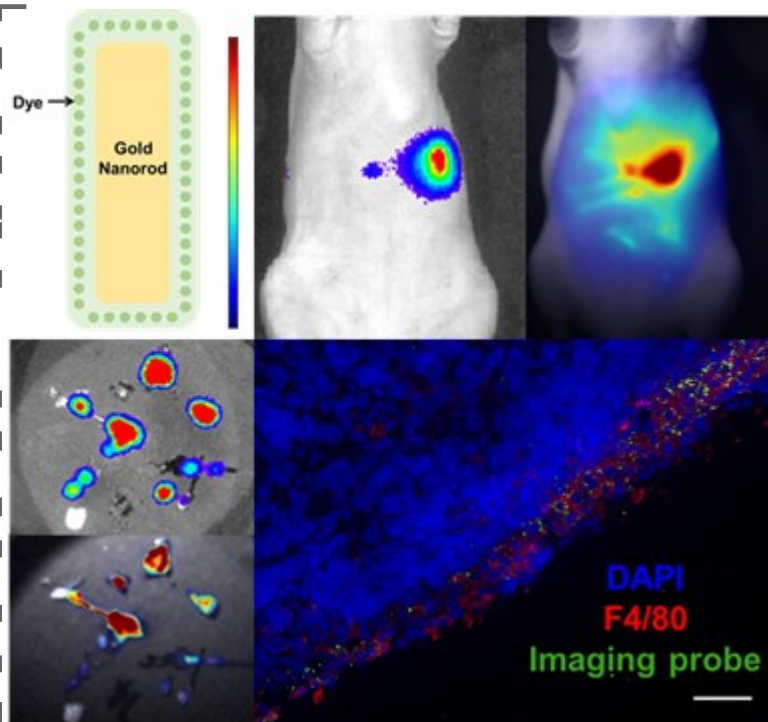
References

[1]   R. Weissleder, M. J. Pittet, *Nature* **2008**, *452*, 580.

[2]   G. Hong, J. C. Lee, J. T. Robinson, U. Raaz, L. Xie, N. F. Huang, J. P. Cooke, H. Dai, *Nat. Med.* **2012**, *18*, 1841.

[3]   H. S. Choi, S. L. Gibbs, J. H. Lee, S. H. Kim, Y. Ashitate, F. Liu, H. Hyun, G. L. Park, Y. Xie, S. Bae, M. Henary, J. V. Frangioni, *Nat. Biotechnol.* **2013**, *31*, 148.

[4]   D. Ghosh, A. F. Bagley, Y. J. Na, M. J. Birrer, S. N. Bhatia, A. M. Belcher, *Proc. Natl. Acad. Sci.* **2014**, *111*, 13948.

[5]   K. Welsher, Z. Liu, S. P. Sherlock, J. T. Robinson, Z. Chen, D. Daranciang, H. Dai, *Nat. Nanotechnol.* **2009**, *4*, 773.

[6]   G. Hong, J. T. Robinson, Y. Zhang, S. Diao, A. L. Antaris, Q. Wang, H. Dai, *Angew. Chemie - Int. Ed.* **2012**, *51*, 9818.

[7]   H. Yi, D. Ghosh, M. H. Ham, J. Qi, P. W. Barone, M. S. Strano, A. M. Belcher, *Nano Lett.* **2012**, *12*, 1176.

[8]   G. Hong, S. Diao, J. Chang, A. L. Antaris, C. Chen, B. Zhang, S. Zhao, D. N. Atochin, P. L. Huang, K. I. Andreasson, C. J. Kuo, H. Dai, *Nat. Photonics* **2014**, *8*, 723.

[9]   N. M. Bardhan, D. Ghosh, A. M. Belcher, *Nat. Commun.* **2014**, *5*, Article #4918.

[10]   C. W. Lin, R. B. Weisman, *Nanomedicine* **2016**, *11*, 2885.

[11]   X. Dang, N. M. Bardhan, J. Qi, L. Gu, N. A. Eze, C. W. Lin, S. Kataria, P. T. Hammond, A. M. Belcher, *Sci. Rep.* **2019**, *9*, 3873.

[12]   C. W. Lin, S. M. Bachilo, M. Vu, K. M. Beckingham, R. Bruce Weisman, *Nanoscale* **2016**, *8*, 10348.

[13]   C. W. Lin, H. Yang, S. R. Sanchez, W. Mao, L. Pang, K. M. Beckingham, R. C. Bast, R. B. Weisman, *ACS Appl. Mater. Interfaces* **2017**, *9*, 41680.

[14]   G. Hong, A. L. Antaris, H. Dai, *Nat. Biomed. Eng.* **2017**, *1*, Article #0010.

[15]   X. Dang, L. Gu, J. Qi, S. Correa, G. Zhang, A. M. Belcher, P. T. Hammond, *Proc. Natl. Acad. Sci.* **2016**, *113*, 5179.

[16]   F. Ding, Y. Zhan, X. Lu, Y. Sun, *Chem. Sci.* **2018**, *9*, 4370.

[17]   N. M. Bardhan, A. M. Belcher, in *Near Infrared-Emitting Nanoparticles Biomed. Appl.*, Springer International Publishing, Cham, **2020**, pp. 231–277.

[18]   C. W. Lin, S. M. Bachilo, Y. Zheng, U. Tsedev, S. Huang, R. B. Weisman, A. M. Belcher, *Nat. Commun.* **2019**, *10*, Article #2874.

[19]   K. Kostarelos, *Nat. Biotechnol.* **2008**, *26*, 774.

[20]   E. Chang, N. Thekkek, W. W. Yu, V. L. Colvin, R. Drezek, *Small* **2006**, *2*, 1412.

[21]   Q. Yang, Z. Ma, H. Wang, B. Zhou, S. Zhu, Y. Zhong, J. Wang, H. Wan, A. Antaris, R. Ma, X. Zhang, J. Yang, X. Zhang, H. Sun, W. Liu, Y. Liang, H. Dai, *Adv. Mater.* **2017**, *29*, 1605497.

[22]   A. L. Antaris, H. Chen, K. Cheng, Y. Sun, G. Hong, C. Qu, S. Diao, Z. Deng, X. Hu, B. Zhang, X. Zhang, O. K. Yaghi, Z. R. Alamparambil, X. Hong, Z. Cheng, H. Dai, *Nat. Mater.* **2016**, *15*, 235.

[23]   W. H. De Jong, P. J. A. Borm, *Int. J. Nanomedicine* **2008**, *3*, 133.

[24]   G. Von Maltzahn, J. H. Park, A. Agrawal, N. K. Bandaru, S. K. Das, M. J. Sailor, S. N. Bhatia, *Cancer Res.* **2009**, *69*, 3892.

[25]   A. M. Alkilany, L. B. Thompson, S. P. Boulos, P. N. Sisco, C. J. Murphy, *Adv. Drug Deliv. Rev.* **2012**, *64*, 190.

[26]   X. Huang, M. A. El-Sayed, *J. Adv. Res.* **2010**, *1*, 13.

[27]   E. C. Dreaden, A. M. Alkilany, X. Huang, C. J. Murphy, M. A. El-Sayed, *Chem. Soc. Rev.* **2012**, *41*, 2740.

[28]   A. M. Gobin, M. H. Lee, N. J. Halas, W. D. James, R. A. Drezek, J. L. West, *Nano Lett.* **2007**, *7*, 1929.

[29]   A. L. Feng, M. L. You, L. Tian, S. Singamaneni, M. Liu, Z. Duan, T. J. Lu, F. Xu, M. Lin, *Sci. Rep.* **2015**, *5*, 7779.

[30]   L. Wang, Q. Song, Q. Liu, D. He, J. Ouyang, *Adv. Funct. Mater.* **2015**, *25*, 7017.

[31]   D. Nepal, L. F. Drummy, S. Biswas, K. Park, R. A. Vaia, *ACS Nano* **2013**, *7*, 9064.

[32]   T. Ming, L. Zhao, Z. Yang, H. Chen, L. Sun, J. Wang, C. Yan, *Nano Lett.* **2009**, *9*, 3896.

[33]   A. M. Gabudean, M. Focsan, S. Astilean, *J. Phys. Chem. C* **2012**, *116*, 12240.

[34]   R. Bardhan, N. K. Grady, J. R. Cole, A. Joshi, N. J. Halas, *ACS Nano* **2009**, *3*, 744.

[35] N. Gandra, C. Portz, L. Tian, R. Tang, B. Xu, S. Achilefu, S. Singamaneni, *Angew. Chemie - Int. Ed.* **2014**, *53*, 866.

[36] T. G. Shutava, S. S. Balkundi, P. Vangala, J. J. Steffan, R. L. Bigelow, J. A. Cardelli, D. P. O'Neal, Y. M. Lvov, *ACS Nano* **2009**, *3*, 1877.

[37] Z. J. Deng, S. W. Morton, E. Ben-Akiva, E. C. Dreaden, K. E. Shopsowitz, P. T. Hammond, *ACS Nano* **2013**, *7*, 9571.

[38] Y. Wang, P. P. Joshi, K. L. Hobbs, M. B. Johnson, D. W. Schmidtke, *Langmuir* **2006**, *22*, 9776.

[39] Z. Tao, X. Dang, X. Huang, M. D. Muzumdar, E. S. Xu, N. M. Bardhan, H. Song, R. Qi, Y. Yu, T. Li, W. Wei, J. Wyckoff, M. J. Birrer, A. M. Belcher, P. P. Ghoroghchian, *Biomaterials* **2017**, *134*, 202.

[40] M. S. Han, C.-H. Tung, *Quant. Imaging Med. Surg.* **2014**, *4*, 156.

[41] L. Ceppi, N. M. Bardhan, Y. Na, A. Siegel, N. Rajan, R. Fruscio, M. G. Del Carmen, A. M. Belcher, M. J. Birrer, *ACS Nano* **2019**, *13*, 5356.

[42] R. Bardhan, W. Chen, M. Bartels, C. Perez-Torres, M. F. Botero, R. W. McAninch, A. Contreras, R. Schiff, R. G. Pautler, N. J. Halas, A. Joshi, *Nano Lett.* **2010**, *10*, 4920.

[43] J.-M. Liu, Y.-Y. Liu, D.-D. Zhang, G.-Z. Fang, S. Wang, *ACS Appl. Mater. Interfaces* **2016**, *8*, 29939.

[44] M. R. K. Ali, Y. Wu, M. A. El-Sayed, *J. Phys. Chem. C* **2019**, *123*, 15375.

[45] O. G. Tovmachenko, C. Graf, D. J. Van Den Heuvel, A. Van Blaaderen, H. C. Gerritsen, *Adv. Mater.* **2006**, *18*, 91.

[46] H. Wan, J. Yue, S. Zhu, T. Uno, X. Zhang, Q. Yang, K. Yu, G. Hong, J. Wang, L. Li, Z. Ma, H. Gao, Y. Zhong, J. Su, A. L. Antaris, Y. Xia, J. Luo, Y. Liang, H. Dai, *Nat. Commun.* **2018**, *9*, Article #1171.

[47] S. Huang, J. Qi, D. W. DeQuilettes, M. Huang, C. W. Lin, N. M. Bardhan, X. Dang, V. Bulović, A. M. Belcher, *Small* **2019**, *15*, 1901233.

[48] C. Yu, J. Irudayaraj, *Anal. Chem.* **2007**, *79*, 572.

[49] X. Song, R. Fu, S. Agathopoulos, H. He, X. Zhao, S. Zhang, *J. Appl. Phys.* **2009**, *106*, 033103.

[50] M. Ringler, A. Schwemer, M. Wunderlich, A. Nichtl, K. Kurzinger, T. A. Klar, J. Feldmann, *Phys. Rev. Lett.* **2008**, *100*, 203002.

[51] P. Anger, P. Bharadwaj, L. Novotny, *Phys. Rev. Lett.* **2006**, *96*, 113002.

[52] C. D. Walkey, J. B. Olsen, H. Guo, A. Emili, W. C. W. Chan, *J. Am. Chem. Soc.* **2012**, *134*, 2139.

[53] K. Siwowska, R. M. Schmid, S. Cohrs, R. Schibli, C. Müller, *Pharmaceuticals* **2017**, *10*, 72.

[54] F. Zhang, G. B. Braun, Y. Shi, Y. Zhang, X. Sun, N. O. Reich, D. Zhao, G. Stucky, *J. Am. Chem. Soc.* **2010**, *132*, 2850.

[55] K. Aslan, M. Wu, J. R. Lakowicz, C. D. Geddes, *J. Am. Chem. Soc.* **2007**, 1524.

[56] P. Wang, Y. Fan, L. Lu, L. Liu, L. Fan, M. Zhao, Y. Xie, C. Xu, F. Zhang, *Nat. Commun.* **2018**, *9*, Article #2898.

[57] Q. Dai, S. Wilhelm, D. Ding, A. M. Syed, S. Sindhwani, Y. Zhang, Y. Y. Chen, P. Macmillan, W. C. W. Chan, *ACS Nano* **2018**, *12*, 8423.

[58] G. Wang, A. S. Stender, W. Sun, N. Fang, *Analyst* **2010**, *135*, 215.

[59] C. Freese, R. E. Unger, R. C. Deller, M. I. Gibson, C. Brochhausen, H. A. Klok, C. J. Kirkpatrick, *Biomater. Sci.* **2013**, *1*, 824.

[60] P. Korangath, J. D. Barnett, A. Sharma, E. T. Henderson, J. Stewart, S. H. Yu, S. K. Kandala, C. T. Yang, J. S. Caserto, M. Hedayati, T. D. Armstrong, E. Jaffee, C. Gruettner, X. C. Zhou, W. Fu, C. Hu, S. Sukumar, B. W. Simons, R. Ivkov, *Sci. Adv.* **2020**, *6*, eaay1601.

[61] T. Motohara, K. Masuda, M. Morotti, Y. Zheng, S. El-Sahhar, K. Y. Chong, N. Wietek, A. Alsaadi, M. Karaminejadranjbar, Z. Hu, M. Artibani, L. S. Gonzalez, H. Katabuchi, H. Saya, A. A. Ahmed, *Oncogene* **2019**, *38*, 2885.